LETTER • OPEN ACCESS

Graphene hot-electron light bulb: incandescence from hBN-encapsulated graphene in air

View the article online for updates and enhancements.

2D Materials

CrossMark

LETTER

Graphene hot-electron light bulb: incandescence from hBN-encapsulated graphene in air

Seok-Kyun Son[1,4], Makars Šiškins[2,4], Ciaran Mullan[2,4], Jun Yin[2], Vasyl G Kravets[2], Aleksey Kozikov[1], Servet Ozdemir[2], Manal Alhazmi[2], Matthew Holwill[1], Kenji Watanabe[3], Takashi Taniguchi[3], Davit Ghazaryan[1,2], Kostya S Novoselov[1,2], Vladimir I Fal'ko[1,2] and Artem Mishchenko[1,2]

1   National Graphene Institute, University of Manchester, Manchester M13 9PL, United Kingdom
2   School of Physics and Astronomy, University of Manchester, Manchester M13 9PL, United Kingdom
3   National Institute for Materials Science, 1-1 Namiki, Tsukuba, 305-0044, Japan
4   These authors contributed equally.

E-mail: artem.mishchenko@gmail.com

Abstract

The excellent electronic and mechanical properties of graphene allow it to sustain very large currents, enabling its incandescence through Joule heating in suspended devices. Although interesting scientifically and promising technologically, this process is unattainable in ambient environment, because graphene quickly oxidises at high temperatures. Here, we take the performance of graphene-based incandescent devices to the next level by encapsulating graphene with hexagonal boron nitride (hBN). Remarkably, we found that the hBN encapsulation provides an excellent protection for hot graphene filaments even at temperatures well above 2000 K. Unrivalled oxidation resistance of hBN combined with atomically clean graphene/hBN interface allows for a stable light emission from our devices in atmosphere for many hours of continuous operation. Furthermore, when confined in a simple photonic cavity, the thermal emission spectrum is modified by a cavity mode, shifting the emission to the visible range spectrum. We believe our results demonstrate that hBN/graphene heterostructures can be used to conveniently explore the technologically important high-temperature regime and to pave the way for future optoelectronic applications of graphene-based systems.

1. Introduction

The concept of van der Waals heterostructures has led to a new technology of layer-by-layer engineering of two-dimensional (2D) materials with atomic precision [1, 2]. Out of the abundance of 2D materials, the two—graphene and hexagonal boron nitride (hBN), still remain the most unique couple, because of their outstanding synergetic properties. The hBN plays a vital role in ultra-high quality graphene devices [3, 4], and as an enabling material for graphene superlattices [5]. Besides, it is also known to protect sensitive 2D materials from environment via encapsulation [6]. Graphene, among its many superlatives, has the highest breakdown current density $j_{max} \sim 10^{12}$ A cm^{-2} (assuming graphene thickness 3.4 Å), as measured in transmission experiments of accelerated (180 keV) xenon ions [7]. In electronic transport devices, the breakdown current densities of graphene are more

modest, reaching ~$5 \cdot 10^8$ A cm^{-2} in a vacuum (and much lower values in air) [8].

The high current-carrying capacity of graphene has made it a simple source of thermal infrared emission [9, 10]. Controlled by a bias voltage, a maximal emission temperature is limited to ~700 K due to heat dissipation to the metallic contacts and to the substrate [8, 10]. The latter mechanism dominates for graphene devices longer than a few microns. In the case of hBN encapsulated graphene devices, heat can also be efficiently dissipated through radiative heat transfer to hBN via its hyperbolic phonon polaritons [11]. Heat transfer is substantially reduced for suspended graphene devices, which leads to much higher emission temperatures approaching 3000 K, and to the emission in the visible spectrum (incandescence) when biased by electrical pulses under high vacuum [12]. But the stability of these devices in air is severely limited due to the oxidation of graphene [8, 12].
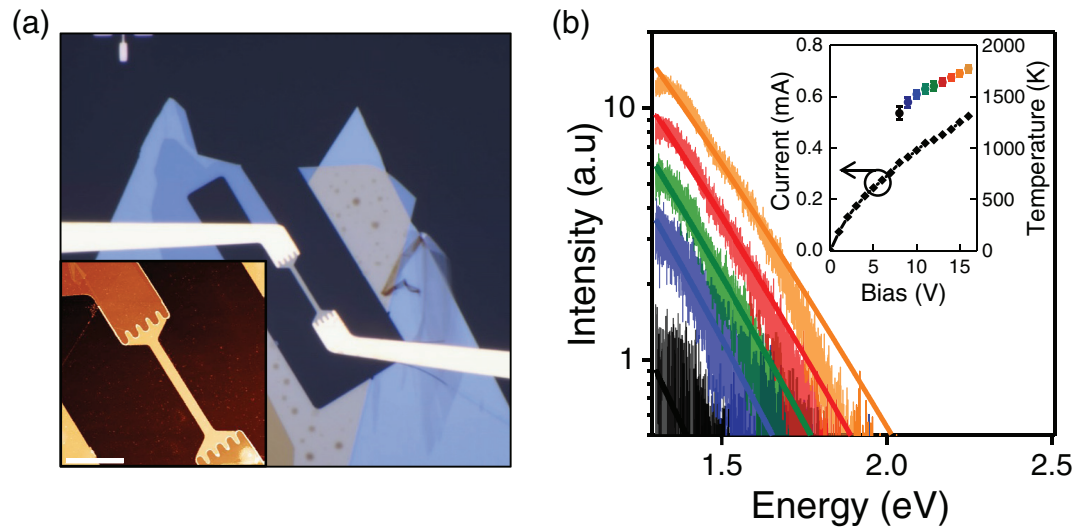
Figure 1. Thermal radiation of Joule-heated hBN/Gr/hBN device on quartz substrate, measured in ambient conditions. (a) Optical micrograph of hBN-encapsulated graphene filament. Inset: AFM image of the same device. Scale bar is 5 μm. (b) Thermal emission spectra from the quartz-supported device at different bias voltages (from 8 V to 16 V with 2 V step, grey to orange). Smooth lines are the fits obtained using equation (1). The inset shows current–voltage characteristics of the device, as well as the electronic temperatures extracted from the fits on the main panel.

Metallic single-walled carbon nanotubes were also used as thermal light emitters, although, small saturation currents (<20 μA for a 3–4 nm diameter nanotube) and rapid oxidation in the air limit their use [13]. Interestingly, the electronic transitions between van Hove singularities led to a strong modification of the emitted spectra [13], which can be tuned even further by employing 1D photonic crystal cavities [14]. In this work, the encapsulation of graphene (Gr) with hBN allowed us to demonstrate robust incandescence of graphene devices in ambient conditions under continuous DC bias over extended periods of time. The hBN encapsulation provides excellent protection for graphene even at temperatures well above 2000 K, which we attribute to an unparalleled oxidation resistance of hBN [15–18]. Our study also reveals that dielectric cavity can support surface-guided waves at visible wavelength and tune the spectra of Planckian radiation.

2. Light emission from hBN-encapsulated graphene

Figure 1(a) shows one of our hBN/Gr/hBN heterostructures fabricated on quartz substrate, using conventional dry peel technology followed by a standard e-beam lithography, dry etching and metallisation, as described elsewhere [4, 19]. We designed our devices such that the distance between the contacts is long enough ($L \sim 10$ μm) to avoid any effects from the contacts while keeping the contact resistance low by increasing the metal-to-graphene contact length. To characterise the light emission we pass a large current I (current density, $j = I/W$, reaching 600 A m^{-1}) through a narrow ($W \sim 1$ μm is the channel width) graphene channel by applying

a bias voltage V_b (estimated electric field $E = V_b/L$ ~ 1.5 V μm^{-1}, where L is the channel length). The supplied electric energy is transformed into Joule heat and dissipated in graphene, encapsulating hBN, quartz substrate, and metallic contacts, leaving a small fraction to radiate into free space. Figure 1(b) shows the emission spectra recorded using Renishaw Raman spectrometer equipped with Si-based CCD detector (diffraction grating 1200/mm; edge filter and beam splitter were removed during measurements). The obtained spectra are mostly featureless and can be described using Planck's law, modified by energy independent emissivity ϵ (grey-body radiation) [9]:

$$I_{\text{grey-body}}(h\nu, T) = \epsilon \frac{2(h\nu)^3}{h^2 c^2} \frac{1}{\exp\left(\frac{h\nu}{k_B T}\right) - 1}, \qquad (1)$$

where $h\nu$ is the photon energy, T is the temperature, c is the speed of light, k_B and h are Boltzmann's and Planck's constants.

Using equation (1) we obtained reasonable fits to the recorded emission spectra; extracted electronic temperatures and corresponding current–voltage characteristics are presented in the inset of figure 1(b). We also evaluated the model for light emission from graphene proposed in [12] but found that the spectra are indistinguishable from grey-body emission in the investigated spectral range. The emission efficiency ($P_{\text{emission}}/P_{\text{electric}}$) of our devices was $\sim 1.6 \cdot 10^{-5}$, obtained using Stefan–Boltzmann law ($P_{\text{emission}} = \epsilon A \sigma T^4$, A—device area, σ—Stefan–Boltzmann constant) and electrical power ($P_{\text{electric}} = IV$) similar to [9, 12]. For the emissivity (ϵ) we used 0.023, following literature [9], the details can be found in the supplementary information (stacks. iop.org/TDM/5/011006/mmedia) (section 3).
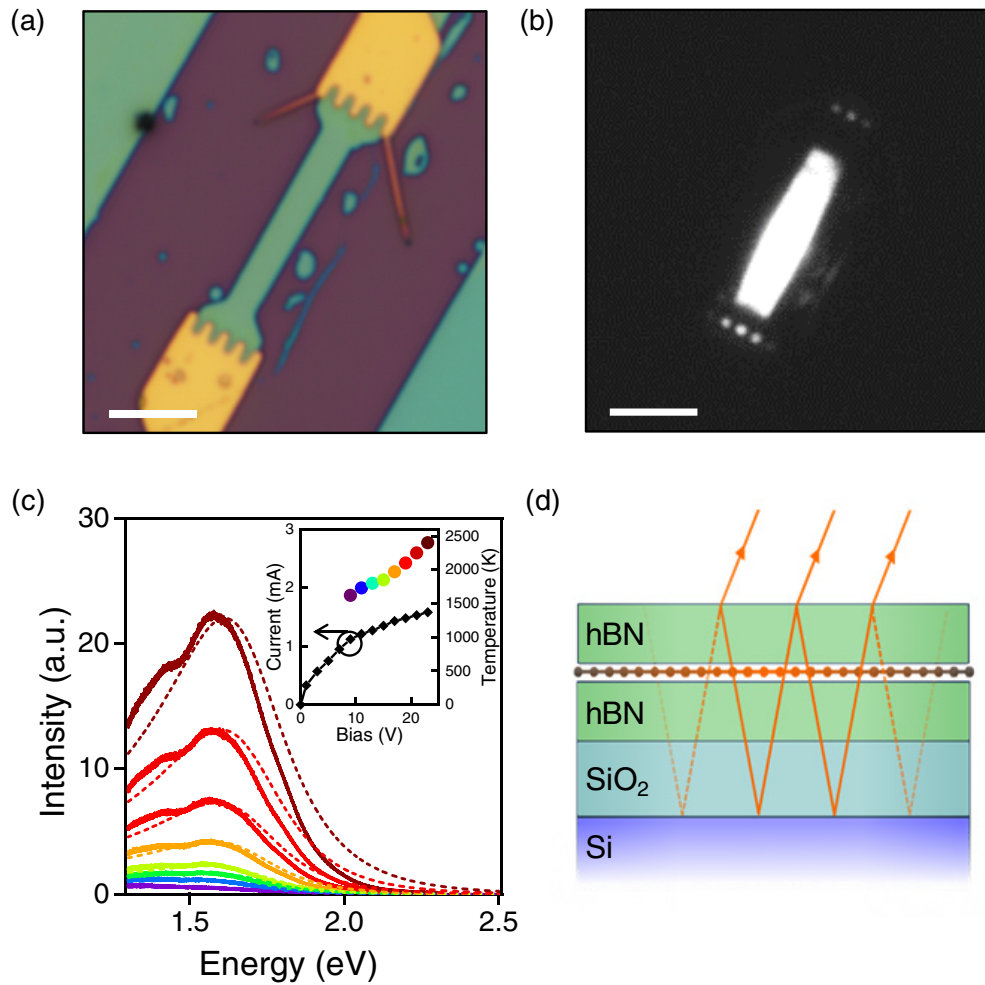
Figure 2. Incandescence in ambient conditions of Joule-heated hBN/Gr/hBN/SiO₂/Si device. (a) Optical micrograph of hBN/Gr/hBN filament under illumination. (b) Its incandescence image captured by a monochrome camera. Scale bars in (a) and (b) are 5 μm. (c) Incandescence spectra (as well as theory curves, equation (2)) of the graphene device at different bias voltages (from 9 V to 23 V in 2 V steps, violet to dark red). The inset shows current–voltage characteristics of the device, as well as the electronic temperatures estimated from photonic cavity model, equation (2). (d) Schematic diagram of a Fabry–Pérot cavity of the air/hBN/Gr/hBN/SiO₂/Si system.

Our devices demonstrated surprising long-term stability (many hours) at these very high current densities ($>1.7 \cdot 10^8$ A cm^{-2}), comparable with multilayer graphene-based infrared emitters but operated at much lower ($7.1 \cdot 10^6$ A cm^{-2}) current densities [10]. We further discuss a long-term stability and the mechanisms of breakdown in the supplementary information (section 1).

3. Enhancement of incandescence using photonic cavity

We prepared another set of hBN/Gr/hBN heterostructures but this time on SiO₂/n-Si substrate and carried out the same high current light emission measurements, figure 2(a). We found that the emission spectra shift to the visible range and the graphene device incandesces (figures 2(b) and (c)). Considering this device is almost identical to that in figure 1, except for the presence of heavily doped silicon substrate, the

drastic change in the emission spectra (see figures 1(b) and 2(c)) can be attributed to a resonance effect of a photonic cavity confined by the two interfaces: hBN/air and SiO₂/Si, figure 2(d).

It is instructive to analyse the parameters of this cavity using a simple model of a Fabry–Pérot resonator [20, 21]. The optical path length of the cavity $D = \sum d_i n_i$ is ~740 nm for 290 nm SiO₂ and 150 nm hBN/Gr/hBN stack. The refractive indices n_i of SiO₂ and hBN show negligible dispersion throughout the visible and near infrared spectral range, averaging at $n_{SiO_2} \sim 1.49$ and $n_{hBN} \sim 2.05$ [20, 22]. The reflectivities R of the 'mirrors' formed by hBN/air and SiO₂/Si interfaces, are 0.12 and 0.19, estimated from Fresnel equations $R_{ij} = \left| \frac{n_i - n_j}{n_i + n_j} \right|^2$, where n_i and n_j are the refractive indices of the materials forming interfaces (with $n_{Si} \sim 3.8$ and $n_{air} = 1$, from [20]). These relatively low reflectivities lead to the output coupling losses, typically parametrised by the mirror coupling coefficients,
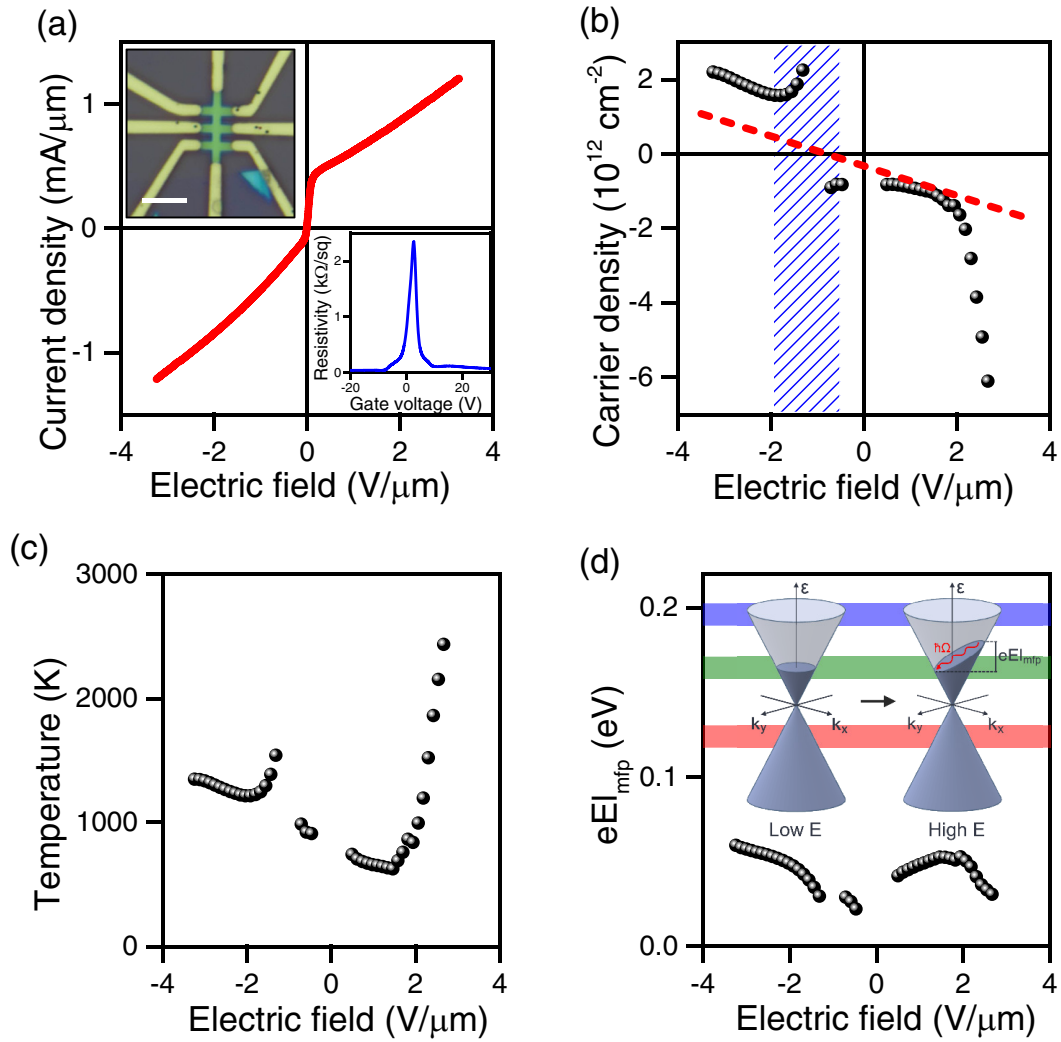
Figure 3. Transport characteristics of a multi-terminal hBN/Gr/hBN Hall bar device, measured in a cryostat at 4 K. (a) Current density j versus electric field E at zero gate voltage. Top inset—device micrograph, scale bar 5 μm. Bottom inset—low-bias resistivity versus gate voltage. (b) Charge carrier density versus electric field (at zero gate voltage) measured from Hall effect (black circles), and estimated from self-gating field effect (dashed red line). The divergence at -1 V μm^{-1} is due to the change in the carrier type (the blue shaded region). (c) Electronic temperature extracted from data on the panel (b) using equation (3). (d) High electric field and high current induced non-equilibrium Fermi distribution limited by electron–phonon scattering processes. The energy values for in-plane graphene phonons (Γ-point optical phonons—blue line, K-point optical phonons—green line, and K-point transversal acoustic phonons—red line) are from phonopy [32].

$\sum -\log(R) = 3.8$ in our case (2.1 and 1.7, for hBN/air and SiO$_2$/Si mirrors, respectively). The expected photon decay time $\tau = t_{RT} / \sum -\log(R) \sim 1.3$ fs ($t_{RT} = 2D/c$ the round trip time for the photon in the cavity) matches well the linewidth ($\Delta E_{measured} \sim 0.5$ eV, see $\Delta E = h/2\pi\tau$) of the measured emission peaks of figure 2(c) (extracted from experimental curves the linewidth values are presented in the figure S7 of the supplementary information). Furthermore, the observed peak maxima (~ 1.6 eV) are very close to the expected second mode of the cavity, $2h/t_{RT} = 1.67$ eV.

We modelled the incandescence spectra by considering the grey-body radiation (equation (1)) modulated by a spectral line shape of the second mode of the cavity (using a Lorentzian, $f(h\nu) = \frac{(\hbar/\tau)^2}{4(h\nu - 2h/t_{RT})^2 + (\hbar/\tau)^2}$, following [21]):

$$I_{cavity}(h\nu, T) = I_{grey\text{-}body}(h\nu, T) f(h\nu). \quad (2)$$

Surprisingly, this simplistic approach provides reasonable quality fits for the data (dashed lines in figure 2(c)), using temperature as the only fitting parameter. The extracted temperatures are presented in the inset of figure 2(c), the values are higher than for the device on quartz (see inset of figure 1(b)) because of the larger electrical power applied in the former case. Our temperatures were somewhat lower (1500–2500 K) in comparison with the emission (2500–2900 K) reported for suspended graphene [12]. We attribute this behaviour to the dissipation of heat to the surrounding media through hBN [11]. The hyperbolic phonon polaritons of hBN [23, 24] are predicted to efficiently (on a picosecond scale) cool hot graphene [11]. To reveal the interplay between the underlying physical mechanisms of cooling one need to perform time-dependent spatially-resolved thermal conductivity measurements, preferably on suspended
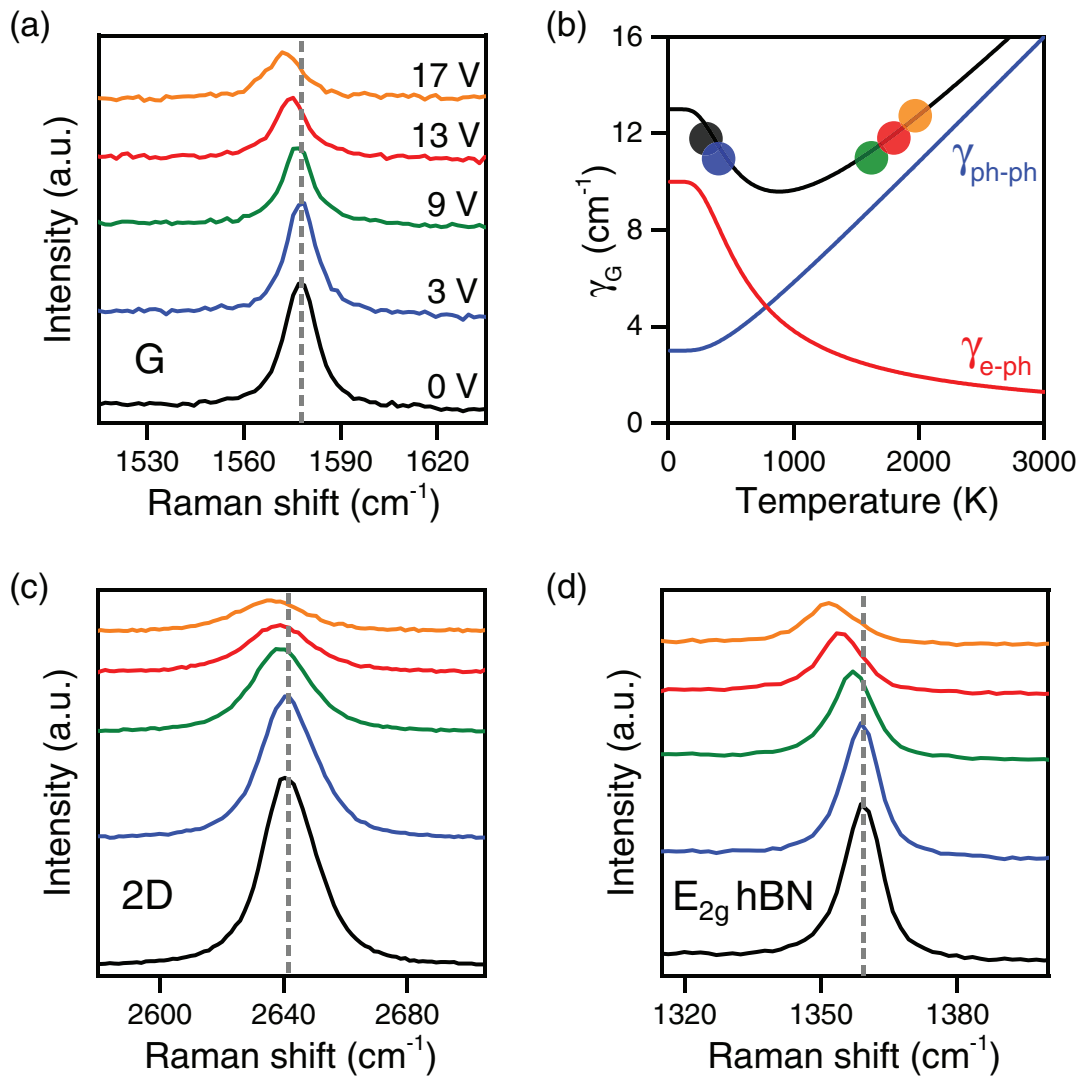
Figure 4. Raman spectra of hBN/Gr/hBN device (same as in figure 2) at different bias voltages. (a) Raman spectra of G peak. (b) The linewidth of G peak as a function of temperature from phonon–phonon lifetime broadening (blue line), electron–hole plasma Landau damping (red line), and their sum (black line). The coloured circles (0–17 V, black to orange) are the experimental points extracted from the panel (a), plotted versus electronic temperatures extrapolated from emission spectra in figure 2. (c) Raman spectra of 2D peak. (d) Raman spectra of E_{2g} hBN peak.

hBN/Gr/hBN heterostructures, which is beyond the scope of this article.

Another effect of the photonic cavity can be seen in figure 2(b)—two rows of bright dots on the opposite ends of the device (their positions coincide with the tips of the gold comb electrodes). The gold electrodes are in thermal equilibrium with environment due to their macroscopic size and very good thermal conductivity, hence the temperature would be too low for the incandescence of the gold tips. On the other hand, the incandescent light from the central area of the device could travel through the waveguide formed by a photonic cavity all the way to the contacts, where it radiates possibly via coupling to gold plasmon modes at the contact edges [25]. The waveguide modes guide the graphene light emission over a long distance (at least 5–10 μm) even in this simple cavity, while the performance can be further improved by optimising the dielectric material and thickness to enhance the light emission [26, 27]. The frequency range of the

photonic cavity modes can also be adjusted by optimising appropriate geometrical and material parameters.

4. Transport measurements in high-bias regime

To better understand the physics of graphene incandescence and to independently estimate the electronic temperatures in a high-bias high-current regime we performed four-terminal transport measurements on an hBN/Gr/hBN Hall bar device, figure 3. Electric field and current density values were obtained from measured 4-probe voltage V_{xx}, applied current I, and the geometry of the Hall bar ($L \times W$ is $2 \times 1 \mu$m^2). At low biases, the current density increases linearly with the electric field and then deviates from the ohmic regime at $|E| > 0.1$ V μm^{-1}, figure 3(a). This saturation tendency is typically attributed to the presence of in-plane acoustic and optical phonons [28–30], and other effects, such as Auger scattering [31].

To estimate the charge carrier density n, we measured our Hall bar device in a perpendicular magnetic field B, following the procedure described in [33]. The transversal voltage V_{xy} was linear with B within the measurement range of ± 2 T, allowing to estimate $n = -IB/eV_{xy}$ at different electric fields, figure 3(b). At a non-zero temperature (T) and in the presence of disorder ($\Delta n < 10^{10}$ cm^{-2}) the measured carrier density is

$$n = \frac{1}{2}\left(n_g + \sqrt{n_g^2 + 4\left(\sqrt{\left(\frac{\Delta n}{2}\right)^2 + (n_{th}(T))^2}\right)^2} \right),$$
(3)

where $n_{th}(T) = \frac{\pi}{6}\left(\frac{k_B T}{\hbar v_F}\right)^2$ is the thermally-induced carrier density, and v_F is the Fermi velocity of electrons in graphene [34, 35]. The gate induced carrier density $n_g = \frac{\varepsilon\varepsilon_0}{de}\Delta V_g$ ($\varepsilon\varepsilon_0$ and d are the dielectric constant and the thickness of gate dielectric) was estimated from the corrected gate voltage ΔV_g, where the self-gating effect (due to large bias voltage) was taken into account, red dashed line in figure 3(b). Using equation (3) we estimated the effective electron temperature of graphene as a function of electric field, figure 3(c). The obtained temperatures are in range with those estimated from the emission spectra (figures 1 and 2).

Knowing the current density j and the charge carrier density n we extracted the drift velocity $v_d = j/ne$, and the mobility $\mu = v_d/E$ at different electric fields (and, hence, temperatures). The v_d slowly saturates starting at $E \sim 1.5$ V μm^{-1} reaching 4×10^5 m s^{-1}, almost 40% of the Fermi velocity. The mobility, high initially ($\sim$100 000 cm^2 V$^{-1}\cdot$s^{-1}), drops to below 1000 cm^2 V$^{-1}\cdot$s^{-1} at high electric fields. From a simple Drude model we approximated the scattering time τ and the mean free path l_{mfp} of the charge carriers from their mobility, $\mu\hbar\sqrt{\pi n}/e = v_F\tau \equiv l_{mfp}$. For independent scattering processes, the scattering time τ is dominated by the shortest process, which at high bias fields is usually the emission of the optical phonons [28, 36]. If the potential difference over the characteristic length l_{mfp} is sufficiently high ($eEl_{mfp} \geqslant \hbar\Omega$) a phonon of energy $\hbar\Omega$ can be emitted resulting in the dissipation (heat) of electric energy in graphene lattice, and surrounding hBN and SiO$_2$. This process, in turn, limits the l_{mfp}, and bounds the non-equilibrium Fermi distribution, as shown on the cartoon in figure 3(d) (depicted as the tilt of the Fermi level). Figure 3(d) compares the characteristic energy eEl_{mfp} against the typical (at high density of states in the phonon dispersion spectra) energies of representative phonon branches of graphene [37, 38]. Interestingly, the obtained characteristic energy values $\sim$60 meV are sufficiently lower than graphene's in-plane phonon excitation energies, figure 3(d). Perhaps low energy acoustic phonons, longitudinal guided modes or other higher order acoustic modes at the interface of hBN and graphene limit the characteristic energy [37]. For a rather thin hBN substrate the characteristic energy might also be bound by optical phonons of SiO$_2$ substrate [28].

5. Raman spectroscopy and lattice temperature

To complement the light emission and transport study, we performed Raman spectroscopy on our hBN/Gr/hBN heterostructures. To this end, we employed the same Renishaw spectrometer using 633 nm excitation laser line with incident power of 2 mW. The recorded spectra of the characteristic Raman peaks (G and 2D for graphene, E_{2g} for hBN) for different bias voltages are summarised in figure 4. The intensities of all three peaks monotonically decrease with temperature. There is also a downshift with increasing temperature for all three peaks: 5 cm^{-1}, 6 cm^{-1}, and 7.5 cm^{-1} for G and 2D peaks of graphene, and E_{2g} peak of hBN at the highest applied bias, respectively. The downshift of the G peak is attributed to the decay of Γ-point optical phonon into acoustic phonons through a range of phonon–phonon scattering processes [39]. Similar anharmonic decay processes (complicated by competing electron–electron scattering) of K-point optical phonons are also responsible for the downshift of the 2D peak of graphene [40, 41]. However, both G and 2D peaks tend to blue-shift as a result of doping [42] and strain [43], thus making it difficult to extract the correct lattice temperature from the Raman peak shift. Furthermore, the linewidth of the 2D peak is also affected by strain, for example, the nanometre-scale strain variations contribute to broadening of the 2D peak [44]. We, therefore, focus below on a linewidth of G peak as the most robust method.

We observed a non-monotonic behaviour of the linewidth $\gamma(T)$ of the Γ-point phonon mode (G peak) with temperature, figures 4(a) and (b). This behaviour is in agreement with previous experimental observations, where linewidth of G peak is also first decreased and then increased with temperature [45]. We follow a simple model, considering two processes by which a Γ-phonon acquires a finite linewidth $\gamma_G(T)$: by the anharmonic decay into two secondary acoustic phonons, $\gamma_{ph-ph}(T)$, or by creating an electron–hole pair (Landau damping), $\gamma_{e-ph}(T,\mu)$ [39, 45]. Here we ignore any higher-order anharmonic coupling processes. The total estimated linewidth of G peak $\gamma_G(T) = \gamma_{e-ph}(T,\mu) + \gamma_{ph-ph}(T)$ is plotted in figure 4(b) (black line; the anharmonic contribution and the Landau damping are the blue and red lines, respectively). We use 10 cm^{-1} and 3 cm^{-1} for $\gamma_{e-ph}(0,0)$ and $\gamma_{ph-ph}(0)$, and include thermally-induced suppression of Landau damping, following procedures from [45, 46]. The γ_G values from figure 4(a) plotted as coloured circles versus electronic temperatures extracted from figure 2(c), are in a good agreement with the simple model suggesting the dominant anharmonic scattering mechanism.

Lastly, the hBN E_{2g} peak is also downshifting and broadening with temperature (figure 4(d)) due to similar anharmonic phonon decay processes in hBN [47]. This suggests there is a strong heat transfer from graphene to the encapsulating hBN. Despite the heat dissipation in the encapsulating hBN layers, the electronic temperatures of graphene were well above 2000 K, as estimated from the incandescence spectra. Understanding the detailed mechanism of heat dissipation through the encapsulating hBN requires further theoretical investigations.

6. Conclusions

We demonstrated an interesting region of a parameter space (high current and electric field, high electronic and lattice temperatures), accessible in simple graphene/hBN heterostructures (and in the majority of existing devices) in ambient conditions. Electrically tunable light emission of graphene is modified by a photonic cavity formed at the interfaces, which can be further improved by optimising the parameters of the cavity. This atomically-thin light source is integrated with the cavity, which forms a waveguide, paving the way for new types of electrically-coupled photonic integrated circuits. This level of integration can be brought even further, by combining the photonic circuit elements with electrically-driven phononic and mechanical modes. We believe our study will stimulate further experimental and theoretical work in this fascinating research direction, where many interesting questions are now open, such as the understanding the mechanisms of heat dissipation in these devices, including the effects of hyperbolic phonon polaritons in hBN.

ORCID iDs

Seok-Kyun Son ⓘ https://orcid.org/0000-0002-9530-2639
Vasyl G Kravets ⓘ https://orcid.org/0000-0003-1895-1106
Artem Mishchenko ⓘ https://orcid.org/0000-0002-0427-5664

References

[1] Geim A K and Grigorieva I V 2013 Van der Waals heterostructures *Nature* **499** 419–25

[2] Novoselov K S, Mishchenko A, Carvalho A and Castro Neto A H 2016 2D materials and van der Waals heterostructures *Science* **353** aac9439

[3] Dean C R *et al* 2010 Boron nitride substrates for high-quality graphene electronics *Nat. Nanotechnol.* **5** 722–6

[4] Wang L *et al* 2013 One-dimensional electrical contact to a two-dimensional material *Science* **342** 614–7

[5] Gorbachev R V *et al* 2014 Detecting topological currents in graphene superlattices *Science* **346** 448–51

[6] Cao Y *et al* 2015 Quality heterostructures from two-dimensional crystals unstable in air by their assembly in inert atmosphere *Nano Lett.* **15** 4914–21

[7] Gruber E *et al* 2016 Ultrafast electronic response of graphene to a strong and localized electric field *Nat. Commun.* **7** 13948

[8] Dorgan V E, Behnam A, Conley H J, Bolotin K I and Pop E 2013 High-field electrical and thermal transport in suspended graphene *Nano Lett.* **13** 4581–6

[9] Freitag M, Chiu H Y, Steiner M, Perebeinos V and Avouris P 2010 Thermal infrared emission from biased graphene *Nat. Nanotechnol.* **5** 497–501

[10] Barnard H R, Zossimova E, Mahlmeister N H, Lawton L M, Luxmoore I J and Nash G R 2016 Boron nitride encapsulated graphene infrared emitters *Appl. Phys. Lett.* **108** 131110

[11] Principi A, Lundeberg M B, Hesp N C, Tielrooij K J, Koppens F H and Polini M 2017 Super-Planckian electron cooling in a van der Waals stack *Phys. Rev. Lett.* **118** 126804

[12] Kim Y D *et al* 2015 Bright visible light emission from graphene *Nat. Nanotechnol.* **10** 676–81

[13] Mann D, Kato Y K, Kinkhabwala A, Pop E, Cao J, Wang X, Zhang L, Wang Q, Guo J and Dai H 2007 Electrically driven thermal light emission from individual single-walled carbon nanotubes *Nat. Nanotechnol.* **2** 33–8

[14] Pyatkov F, Futterling V, Khasminskaya S, Flavel B S, Hennrich F, Kappes M M, Krupke R and Pernice W H P 2016 Cavity-enhanced light emission from electrically driven carbon nanotubes *Nat. Photon.* **10** 420

[15] Liu Z *et al* 2013 Ultrathin high-temperature oxidation-resistant coatings of hexagonal boron nitride *Nat. Commun.* **4** 2541

[16] Yi M, Shen Z G, Zhao X H, Liang S S and Liu L 2014 Boron nitride nanosheets as oxygen-atom corrosion protective coatings *Appl. Phys. Lett.* **104** 143101

[17] Shen L T, Zhao Y D, Wang Y, Song R B, Yao Q, Chen S S and Chai Y 2016 A long-term corrosion barrier with an insulating boron nitride monolayer *J. Mater. Chem.* A **4** 5044–50

[18] Galbiati M, Stoot A C, Mackenzie D M, Boggild P and Camilli L 2017 Real-time oxide evolution of copper protected by graphene and boron nitride barriers *Sci. Rep.* **7** 39770

[19] Tien D H, Park J Y, Kim K B, Lee N, Choi T, Kim P, Taniguchi T, Watanabe K and Seo Y 2016 Study of graphene-based 2D-heterostructure device fabricated by all-dry transfer process *ACS Appl. Mater. Interfaces* **8** 3072–8

[20] Tompkins H and Irene E A 2005 *Handbook of Ellipsometry* (New York: Elsevier)

[21] Ismail N, Kores C C, Geskus D and Pollnau M 2016 Fabry–Perot resonator: spectral line shapes, generic and related Airy distributions, linewidths, finesses, and performance at low or frequency-dependent reflectivity *Opt. Express* **24** 16366–89

[22] Franke E, Schubert M, Hecht J D, Neumann H, Tiwald T E, Thompson D W, Yao H, Woollam J A and Hahn J 1998 *In situ* infrared and visible-light ellipsometric investigations of boron nitride thin films at elevated temperatures *J. Appl. Phys.* **84** 526–32

[23] Caldwell J D *et al* 2014 Sub-diffractional volume-confined polaritons in the natural hyperbolic material hexagonal boron nitride *Nat. Commun.* **5** 5221

[24] Dai S *et al* 2014 Tunable phonon polaritons in atomically thin van der Waals crystals of boron nitride *Science* **343** 1125–9

[25] Gryczynski I, Malicka J, Gryczynski Z and Lakowicz J R 2004 Surface plasmon-coupled emission with gold films *J. Phys. Chem.* B **108** 12568–74

[26] Blake P, Hill E W, Castro Neto A H, Novoselov K S, Jiang D, Yang R, Booth T J and Geim A K 2007 Making graphene visible *Appl. Phys. Lett.* **91** 063124

[27] Abergel D S L, Russell A and Fal'ko V I 2007 Visibility of graphene flakes on a dielectric substrate *Appl. Phys. Lett.* **91** 063125

[28] Meric I, Han M Y, Young A F, Ozyilmaz B, Kim P and Shepard K L 2008 Current saturation in zero-bandgap, top-gated graphene field-effect transistors *Nat. Nanotechnol.* **3** 654–9

[29] Perebeinos V and Avouris P 2010 Inelastic scattering and current saturation in graphene *Phys. Rev. B* **81** 195442

[30] Dorgan V E, Bae M H and Pop E 2010 Mobility and saturation velocity in graphene on SiO₂ *Appl. Phys. Lett.* **97** 082112

[31] Winzer T, Jago R and Malic E 2016 Experimentally accessible signatures of Auger scattering in graphene *Phys. Rev. B* **94** 235430

[32] Togo A and Tanaka I 2015 First principles phonon calculations in materials science *Scr. Mater.* **108** 1–5

[33] Pan J, Zhang H J, Zheng Y, Zhang B, Zhang T and Sheng P 2016 Spatial variation of charge carrier density in graphene under a large bias current *Phys. Rev. B* **93** 115424

[34] Mayorov A S, Elias D C, Mukhin I S, Morozov S V, Ponomarenko L A, Novoselov K S, Geim A K and Gorbachev R V 2012 How close can one approach the Dirac point in graphene experimentally? *Nano Lett.* **12** 4629–34

[35] Mayorov A S *et al* 2011 Interaction-driven spectrum reconstruction in bilayer graphene *Science* **333** 860–3

[36] Barreiro A, Lazzeri M, Moser J, Mauri F and Bachtold A 2009 Transport properties of graphene in the high-current limit *Phys. Rev. Lett.* **103** 076601

[37] Vdovin E E *et al* 2016 Phonon-assisted resonant tunneling of electrons in graphene-boron nitride transistors *Phys. Rev. Lett.* **116** 186603

[38] Fratini S and Guinea F 2008 Substrate-limited electron dynamics in graphene *Phys. Rev. B* **77** 195415

[39] Bonini N, Lazzeri M, Marzari N and Mauri F 2007 Phonon anharmonicities in graphite and graphene *Phys. Rev. Lett.* **99** 176802

[40] Berciaud S, Han M Y, Mak K F, Brus L E, Kim P and Heinz T F 2010 Electron and optical phonon temperatures in electrically biased graphene *Phys. Rev. Lett.* **104** 227401

[41] Basko D M, Piscanec S and Ferrari A C 2009 Electron–electron interactions and doping dependence of the two-phonon Raman intensity in graphene *Phys. Rev. B* **80** 165413

[42] Das A *et al* 2008 Monitoring dopants by Raman scattering in an electrochemically top-gated graphene transistor *Nat. Nanotechnol.* **3** 210–5

[43] Frank O, Tsoukleri G, Parthenios J, Papagelis K, Riaz I, Jalil R, Novoselov K S and Galiotis C 2010 Compression behavior of single-layer graphenes *ACS Nano* **4** 3131–8

[44] Neumann C *et al* 2015 Raman spectroscopy as probe of nanometre-scale strain variations in graphene *Nat. Commun.* **6** 8429

[45] Chae D H, Krauss B, von Klitzing K and Smet J H 2010 Hot phonons in an electrically biased graphene constriction *Nano Lett.* **10** 466–71

[46] Lin J, Guo L, Huang Q, Jia Y, Li K, Lai X and Chen X 2011 Anharmonic phonon effects in Raman spectra of unsupported vertical graphene sheets *Phys. Rev. B* **83** 125430

[47] Cusco R, Gil B, Cassabois G and Artus L 2016 Temperature dependence of Raman-active phonons and anharmonic interactions in layered hexagonal BN *Phys. Rev. B* **94** 155435